Vessels as 4-D Curves: Global Minimal 4-D Paths to Extract 3-D Tubular Surfaces and Centerlines

Hua Li and Anthony Yezzi*

***Abstract*—In this paper, we propose an innovative approach to the segmentation of tubular structures. This approach combines all of the benefits of minimal path techniques such as global minimizers, fast computation, and powerful incorporation of user input, while also having the capability to represent and detect vessel surfaces directly which so far has been a feature restricted to active contour and surface techniques. The key is to represent the trajectory of a tubular structure not as a 3-D curve but to go up a dimension and represent the entire structure as a 4-D curve. Then we are able to fully exploit minimal path techniques to obtain global minimizing trajectories between two user supplied endpoints in order to reconstruct tubular structures from noisy or low contrast 3-D data without the sensitivity to local minima inherent in most active surface techniques. In contrast to standard purely spatial 3-D minimal path techniques, however, we are able to represent a full tubular surface rather than just a curve which runs through its interior. Our representation also yields a natural notion of a tube's "central curve." We demonstrate and validate the utility of this approach on magnetic resonance (MR) angiography and computed tomography (CT) images of coronary arteries.**

***Index Terms*—Eikonal equations, fast marching techniques, geodesic active contours, global minima, minimal path methods.**

I. Introduction

MEDICAL image segmentation is an essential, primary, and important step for clinical tasks such as 3-D organ visualization, disease diagnosis, and surgical planning. Numerous segmentation methods have been proposed that depend upon organ structures, imaging modalities, application domains, user-interaction requirements, and so on [1]–[5]. The extraction of vascular objects such as blood vessels, coronary arteries, and retinal blood vessels, has attracted the attention of more and more researchers.

Generally, vascular structures are treated as tubular structures, and most proposed vessel extraction methods are based on this assumption. With different segmentation objectives, existing vessel extraction methods can be divided into two categories: surface extraction methods and centerline (or skeleton) extraction methods. Here, we give a brief review of some representative methods on vessel surface extraction or centerline extraction, and focus specifically on the methods based on active contour models [6]–[8] and minimal path techniques [9], [10], because the approach proposed in this paper combines all of the benefits of minimal path techniques, while also having the full representation power of active contour and surface techniques. More detailed descriptions of a number of methods for vessel surface or centerline extraction can be found in [3]–[5].

Surface extraction methods have been proposed to extract vessel surfaces directly followed by thinning or similar algorithms to generate the corresponding centerlines. Deformable models (or active contour models) with various constraints have been widely used in this category. Frangi *et al.* [11] presented a parametric deformable model, which consists of the representation of the central vessel axis coupled to a vessel wall surface, for quantitatively defining vessel boundaries of 3-D magnetic resonance angiogram (MRA) data. However, parametric deformable models are not powerful tools for detecting complex vascular structures accurately because they cannot handle topological changes during surface evolution. Shortly afterward, a geodesic active contour model for the segmentation of brain vascular structures and abdominal aortas from MRA or computed tomography (CT) images was designed in [12], in which the energy is minimized based on the image intensity values together with the local smoothness properties of the desired boundary. Another active contour model [13] utilizes the central vessel axis obtained from the multiscale filtering technique in [11] to initialize a level set evolution for the segmentation of contrast-enhanced MRA data.

In contrast to using deformable models alone, some researchers have also integrated them with different preprocessing or postprocessing operators. In [14], the authors interactively activated three terms in the level set evolution equation for segmenting the interesting MRA vessels of a whole vascular tree, and also refined the resulting models for computational fluid dynamics simulations. Similarly, Chan *et al.* [15] combined multiscale filtering, deformable geometric models, and level set evolution for the segmentation, correction, reconstruction, and quantification of vessel structures from 3-D MRA image data. In [16], triangulated meshes are integrated with a special deformable isosurface model to conform to the boundaries of objects with *a priori* assumptions of object shape. Based on Bayesian principles and level set evolutions, an approach [17] was developed for the 3-D segmentation and reconstruction of human left coronary arteries from angio-CT data. Unlike the method in [17], Nain [18] used an implicit deformable model with a soft shape prior for vessel segmentation. Manniesing [19] utilized an estimation of the background and vessel inten-

Manuscript received May 27, 2007; revised June 27, 2007. This work was supported in part by the NSF under Grant CCR-0133736 and in part by the NIH/NINDS under Grant R01-NS-037747. *Asterisk indicates corresponding author.*

H. Li was with the School of Electrical and Computer Engineering, Georgia Institute of Technology, Atlanta, GA 30332 USA. She is now with the Department of Radiation Oncology, Washington University, St. Louis, MO 63110 USA (e-mail: huali@radonc.wustl.edu).

*A. Yezzi is with the School of Electrical and Computer Engineering, Georgia Institute of Technology, Atlanta, GA 30332 USA (e-mail: ayezzi@ece.gatech.edu).

Color versions of one or more of the figures in this paper are available online at http://ieeexplore.ieee.org.

Digital Object Identifier 10.1109/TMI.2007.903696

sity distributions to guide the level set evolution for cerebral vascular tree segmentation from computed tomography angiography (CTA) data. A capillary geodesic active contour which utilizes capillary forces was introduced in [20] to detect very thin blood vessel branches. In these methods, initializations must be performed carefully, which is also a common trait of variational active contour models. However, the initialization of our method simply consists of choosing two spherical endpoints of the vessel to be extracted. Beyond these deformable models, other methods reported during the past twenty years include statistical models [21], active shape models [22], nonlinear anisotropic filtering methods [23], multiple scale filtering methods [24], edge operator methods [25], topology marking methods [26], mathematical morphology [27], region-growing [28], vessel tracking [29], and *a priori* anatomical knowledge based methods [30].

Contrary to contour or surface based techniques, centerline extraction methods have been proposed to extract only a centerline (or skeleton), thereby requiring further processing to obtain the 3-D surface or shape. By assuming the centerline corresponds to a kind of minimal cost path, some methods have been designed based on path finding procedures. Wink *et al.* [31] developed a multiscale approach for determining the central axis of vessels in 2-D and 3-D images based on the minimum cost path program [32]. In another skeletonization algorithm proposed by Bouix *et al.* [33], the average outward flux of the gradient vector field of a Euclidean distance function from the structure boundary is calculated based on the skeletonization method proposed in [34]. Deschamps and Cohen [35] simplified the problem of generating centerlines into the problem of finding minimal paths [9], [10] in 3-D images by fast marching methods [36]. Although their method is most closely related to our method, it can only detect a simple curve, while our method has the advantage of detecting vessel surfaces and centerlines simultaneously while maintaining all of the benefits of the minimal path technique. A number of other centerline extraction methods have also been reported in the literature, such as 3-D parallel curve-thinning algorithms [37], methods based on Euclidean distance transformations [38], multiscale filtering methods [39], and iterative centerline tracking approaches based on Hessian matrix [40].

However, to the best of our knowledge, none of the reported techniques inherit the elegant advantage of detecting vessel surfaces and centerlines simultaneously. In this paper, we propose a novel tubular structure extraction method which is very different than the other methods introduced above. Although our method is motivated by minimal path techniques [10], we instead propose a novel variant of the traditional, purely spatial minimal path technique by incorporating an additional *nonspatial* dimension into the search space. The resulting algorithm requires us to search for a *single*, global minimal path between user supplied endpoints in this higher dimensional domain. The detected path captures directly and simultaneously the *central curve* of the extracted vessel as well as the 3-D *vessel surface*. As such, we keep all of the benefits of purely spatial minimal path techniques as well as one of the primary benefits of active contour and surface evolution techniques.

The key is to model a vessel, or any other tubular surface, as a 4-D curve rather than a purely spatial 3-D curve. Each point on the 4-D curve consists of three spatial coordinates plus a fourth coordinate which describes the thickness (radius) of the vessel at that corresponding 3-D point in space. Thus, each 4-D point represents a sphere in 3-D space, and the vessel is obtained by taking the envelope of these spheres as we move along the 4-D curve. We may instead take the center points of this family of spheres if we wish to reconstruct the central path rather than the surface of the detected tubular structure. Like traditional spatial minimal path algorithms, we may exploit techniques such as fast marching methods to keep the computation time down. The implementation is a straightforward 4-D version of the 3-D implementation, and is, therefore, extremely simple. The initial user-supplied endpoints are also very useful in avoiding spurious side branches. Finally, we demonstrate the utility of this approach on both 2-D and 3-D MR angiography and CT coronary images.

II. Tubular Surface Extraction

A. Background—Global Minimal Paths

The minimal path technique proposed in [10] captures the global minimum curve of a contour dependent energy between two user supplied endpoints. The well-known snake model [6] combines smoothing terms and an image feature term (potential P) in the energy functional

$$E(C)=\alpha\int_0^1 \|C'(s)\|^2\,ds+\beta\int_0^1 \|C''(s)\|^2\,ds+\lambda\int_0^1 P(C(s))ds \tag{1}$$

where α, β, and λ are real positive weighting constants, $C(s)\in\mathbb{R}^n$ is a parameterized curve, $C'(s)$ is the first derivative and $C''(s)$ the second derivative with respect to s, and $P(C)$ is a potential which depends upon some desirable image features. In the minimal path technique, contrary to (1), a simplified energy minimization model

$$E(C)=\int_\Omega \{\omega+P(C(s))\}\,ds=\int_\Omega \widetilde{P}(C)ds \tag{2}$$

was proposed without the second derivative term. In this model, s represents the arc-length parameter, $C(s)\in\mathbb{R}^n$ represents a curve, P is the potential associated to the image, ω is a real positive constant, and $\widetilde{P}=P+\omega$. $E(C)$ represents the energy along the curve C.

Given a potential $P>0$ that takes lower values near the desired boundary, the objective of the minimal path technique is to look for a path (connecting two user-supplied end points) along which the integral of $\widetilde{P}=P+\omega$ is minimal. A minimal action map $U_{p_0}(p)$ is defined as the minimal energy integrated along a path between a starting point p_0 and any point p

$$U_{p_0}(p)=\inf_{A_{p_0,p}}\left\{\int_\Omega \widetilde{P}(C(s))\,ds\right\}=\inf_{A_{p_0,p}}\{E(C)\} \tag{3}$$

where $A_{p_0,p}$ is defined as the set of all paths between p_0 and p. The value at each point p of this minimal action map $U_{p_0}(p)$ corresponds to the minimal energy integrated along a path starting from point p_0 to point p. Thus, the minimal path between point

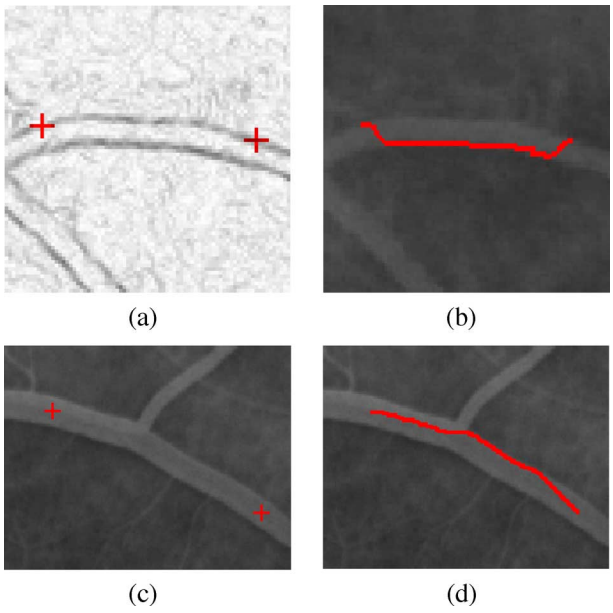

Fig. 1. Two disadvantages of the classical minimal path technique. Panel (a) shows the gradient information and the two initial points (red crosses). Panel (b) shows the related original image with the extracted boundary (red line). Panel (c) shows another original image and the two initial points (red crosses). Panel (d) shows the extracted inaccurate central path (red line).

p_0 and point p can be easily deduced by calculating the action map $U_{p_0}(p)$ and then sliding backwards along its gradient field from point p to point p_0. Because the action map U_{p_0} has only one minimum value at the starting point p_0 and increases from p_0 outward, it can be determined by solving the Eikonal equation

$$\|\nabla U_{p_0}\| = \widetilde{P} \quad \text{with} \quad U_{p_0}(p_0) = 0. \tag{4}$$

Three algorithms are described in [10] to compute this map U_{p_0} which are all consistent with the continuous propagation rule while implemented on a rectangular grid. These three algorithms utilize level set methods [41], shape from shading methods [42], [43], and fast marching methods [44]. Fast marching methods were favored because of their lower complexity compared to the other two algorithms.

The minimal path approach [10] has several advantages such as finding global minimizers, fast computation, ease of implementation, and more powerful incorporation of user input. Such advantages are lacking in most surface evolution techniques (whether they be level set or finite element approaches) with the problem of local minima being particularly troublesome in most cases. Surface evolution approaches generally make use of user input only for obtaining seed points from which to start evolving the initial surface. This is fundamentally different from minimal path techniques which are specifically designed to fully trust and exploit the initial user input, guaranteeing its incorporation into the final answer. Unfortunately, despite their numerous advantages, traditional minimal path techniques exhibit some disadvantages both in general and in the particular application of vessel segmentation.

First, *vessel boundary* extraction can be exceedingly difficult, even in 2-D where the longitudinal cross-sectional boundary of a vessel is completely described by two curves (see Fig. 1). Even if the two user-supplied endpoints are located exactly on the same desired boundary, the minimal path may jump temporarily to a different nearby boundary and return at a later point as a "short cut" to reduce the total cost of the path. This is illustrated in Fig. 1(a) and (b). However, surface evolution techniques do have one nice advantage, though: when they are successful, they capture and represent the vascular surface directly, not just some path running through its interior as in the minimal path approach. This is particularly important in cases where one wishes to measure changes in vascular thickness at different places along the vessel.

Second, *vessel interior* extraction does not always yield a trajectory that remains central to the vessel. Since intensity based potentials do not vary greatly between different points within the vessel interior, the minimal path tends to favor trajectories of shortest Euclidean distance within the tubular structure, often yielding paths that run tangential to vessel boundaries rather than central to their interior. This undesirable property is shown here in Fig. 1(c) and (d), and later in Fig. 3(f) and (l). This affects applications such as virtual endoscopy, where subsequent path centering methods [35] are required to readjust a traditionally extracted, purely spatial minimal path in order to obtain a central trajectory for virtual fly-through.

Finally, in 3-D (just as in 2-D), traditional purely spatial minimal path techniques can be used only for curve extraction, whereas vessels and other tubular structures, despite sharing some characteristics with curves, are surfaces. In [45], the authors proposed a 3-D surface extraction method. It models the desired surface as an infinite set of 3-D minimal paths that join individual points between two user supplied curves. Their approach, which is not designed for vessels, would struggle in capturing long winding vessel boundaries, for the reasons illustrated in Fig. 1(a) and (b), and has a complex implementation.

B. Generalization: Tubular Surface Extraction

As discussed in Section II-A, traditional *spatial* minimal path techniques do not apply for the detection of surfaces or regions. However, for the special case of vessels and other tubular surfaces, we may generalize these approaches by representing a *3-D vessel surface* as a *4-D curve* and using a corresponding minimal path algorithm in 4-D. As such, we keep all of the benefits of minimal path techniques (global minima, fast implementations, full incorporation of user input) while adding the ability to represent and detect the vessel surface directly, which so far has been a feature restricted to active contour and active surface techniques.

We represent the surface of a tubular structure as the envelope of a one-parameter family (curve) of spheres with different centers (three coordinates) and different radii (fourth coordinate). This representation is illustrated in Fig. 2. In this way, the *3-D surface* extraction problem is translated into the problem of finding a *4-D curve* which encodes this family of 3-D spheres.

We now modify (2) to a new energy minimization model relating to 3-D spheres rather than 3-D points

$$E(\hat{C}) = \int_{\Omega} \left\{ \omega + P\left(\hat{C}\left(c(s), r(s)\right)\right) \right\} ds = \int_{\Omega} \widetilde{P}(\hat{C}) ds \tag{5}$$

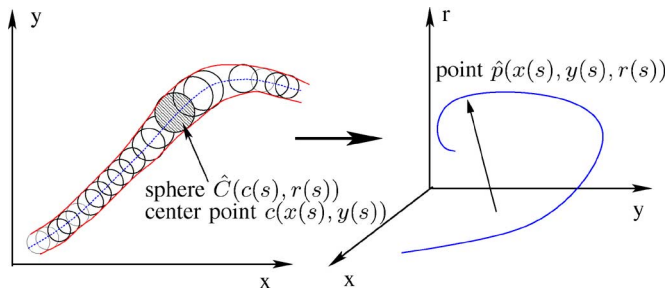

Fig. 2. We present a tubular surface as the envelope of a family of spheres with continuously changing center points and radii.

where s still represents the arc-length parameter over an interval Ω, $c(s)$ represents the location of a point in the original image domain Ω_I either in $\mathbb{R}^2[c(s) = (x(s), y(s))]$ or in $\mathbb{R}^3[c(s) = (x(s), y(s), z(s))]$, $r(s) \in [0, r_{\max}]$ represents the radius of a circle/sphere centered at $c(s)$ ($r_{\max}$ is the largest allowed thickness of the vessel to be captured), $\hat{C}(c(s), r(s)) \in \Omega_I$ represents a "path" composed by a family of circles/spheres in Ω_I, $E(\hat{C})$ represents the energy which is the integral of $\widetilde{P}$ along $\hat{C}(c(s), r(s))$, P is the potential related to the image properties, ω is a real positive constant, and $\widetilde{P} = P + w$.

Furthermore, in (5), ds is a differential displacement vector and $ds^2 = dx^2 + dy^2 + dz^2 + \lambda dr^2$. r represents the sphere radius, and it may have the different Euclidean metric. λ imposes a smoothness constraint on the variations of the sphere radius and may be changed. We simply choose $\lambda = 1$ for all the tests in this paper.

Traditionally, the potential $\widetilde{P}$ is a *pointwise* image measurement. Here, we instead design $\widetilde{P}$ as a measurement which incorporates the full set of image values within a sphere. We define a sphere in Ω_I as $sp = (p, r)$, where p is the center point and r is the radius. In designing $\widetilde{P}$ related to such spheres in the image, we should keep in mind that the entire sphere should lie inside the desired object and be as large as possible (so that it is tangential to the object boundary). Such spheres should exhibit lower values of $\widetilde{P}$ compared to smaller spheres which lie inside the desired object or any sphere which lies outside (fully or partially) the desired object.

Given a potential $\widetilde{P}$ that satisfies the above conditions (we will give two example potentials later) and two user supplied spheres sp_0 and sp_1 which mark the beginning and ending locations (and radii) of the vessel or tubular object, our goal is to find a family of spheres $\hat{C}$ such that $\hat{C}(c(0), r(0)) = sp_0$ and $\hat{C}(c(1), r(1)) = sp_1$ and such that the integral of $\widetilde{P} = P + \omega$ along $\hat{C}$ is minimal. The vessel interior is then modeled by the union of the interiors of all the spheres along $\hat{C}$, its surface is modeled by the envelope of the spheres along $\hat{C}$, and its centerline is modeled by the centers of the spheres along $\hat{C}$. In addition, the varying thickness of the vessel may be read directly using the radii of the spheres along $\hat{C}$.

There are two problems to solve in this proposed method. The first is how to minimize the energy functional shown in (5). In particular, can we still define the minimal action map and use fast marching methods to calculate it? The second one is how to formulate an appropriate potential $\widetilde{P}$ satisfying the discussed design conditions.

A sphere $sp = (p, r)$ in Ω_I corresponds to a point $\hat{p}$ in a new domain $\Omega_{I,r} = \Omega_I \times [0, r_{\max}]$. Here, the sphere's radius $r \in \mathbb{R}^1$ is added as the additional fourth coordinate in $\Omega_{I,r}$. In this way, each point in $\Omega_{I,r}$ consists of three spatial coordinates of a 3-D sphere's center plus a fourth coordinate which represents its radius. The initial 3-D sphere sp_0 is the 4-D point $\hat{p}_0$, and the final 3-D sphere sp_1 is the 4-D point $\hat{p}_1$. The problem of finding a family of spheres $\hat{C}$ in 3-D is translated to the problem of finding an optimal curve in 4-D with $\hat{p}_0$ and $\hat{p}_1$ as its end points (optimal meaning that along this 4-D path the integral of $\widetilde{P} = P + \omega$ is minimal). So, we are able to fully exploit the minimal path technique to obtain minimizing trajectories between two 4-D end-points. Since a 2-D (or 3-D) sphere is represented as a point in 3-D (or 4-D), we should use a 3-D (or 4-D) fast marching scheme to solve the Eikonal equation and calculate the minimal action map of 2-D (or 3-D) spheres.

C. Analysis of the Proposed Method

Our tubular surface extraction method is very simple once the observation that a 3-D tubular surface can be modeled as a 4-D curve is made. As such, we may use very standard numerical algorithms to calculate a minimal path in one higher dimension to obtain a direct representation of the tubular surface itself. In this section, we offer some choices for the 4-D potential $\widetilde{P}$ as well as address the front propagation scheme, the algorithm complexity, and the relationship between our method with purely spatial minimal path techniques.

An appropriate potential $\widetilde{P}$ is the most important factor for obtaining accurate surface extraction results. P is an image feature attraction item and should be decided according to the properties of the images. We expect that $\widetilde{P}$ yields the smallest values for largest possible spheres which are fully inside the desired object. For tubular objects in medical imaging such as vessels and colons, the intensity inside the objects is often fairly constant (at least within small sections of the "tube"). We may exploit this property to design the first sample potential.

For any image point p with gray value $I(p)$ in an image I, we define the mean value $\mu(sp)$ and the variance $\sigma^2(sp)$ of sphere $sp = (p, r)$ as

$$\mu(sp) = \frac{\int_{B(p,r)} I(\widetilde{p}) d\widetilde{p}}{\int_{B(p,r)} d\widetilde{p}}$$
$$\sigma^2(sp) = \frac{\int_{B(p,r)} \left(I(\widetilde{p}) - \mu(sp)\right)^2 d\widetilde{p}}{\int_{B(p,r)} d\widetilde{p}} \tag{6}$$

where $B(p, r)$ represents the whole sphere. We then propose a sample potential

$$\begin{aligned}\widetilde{P}(\hat{p}) &= \widetilde{P}(sp) \\ &= \omega + \lambda_1 \left(\left| \mu(sp)/r - \mu(sp_0)/r \right|^2 \right) \\ &\quad + \lambda_2 \left(\left| \sigma^2(sp)/r - \sigma^2(sp_0)/r \right|^2 \right)\end{aligned} \tag{7}$$

where $\mu(sp_0)$ and $\sigma^2(sp_0)$ represent the mean and the variance of the starting sphere sp_0, ω is a real positive constant to control the smoothness of the obtained path, and λ_1 and λ_2 are two real positive weights for the mean difference and variance difference

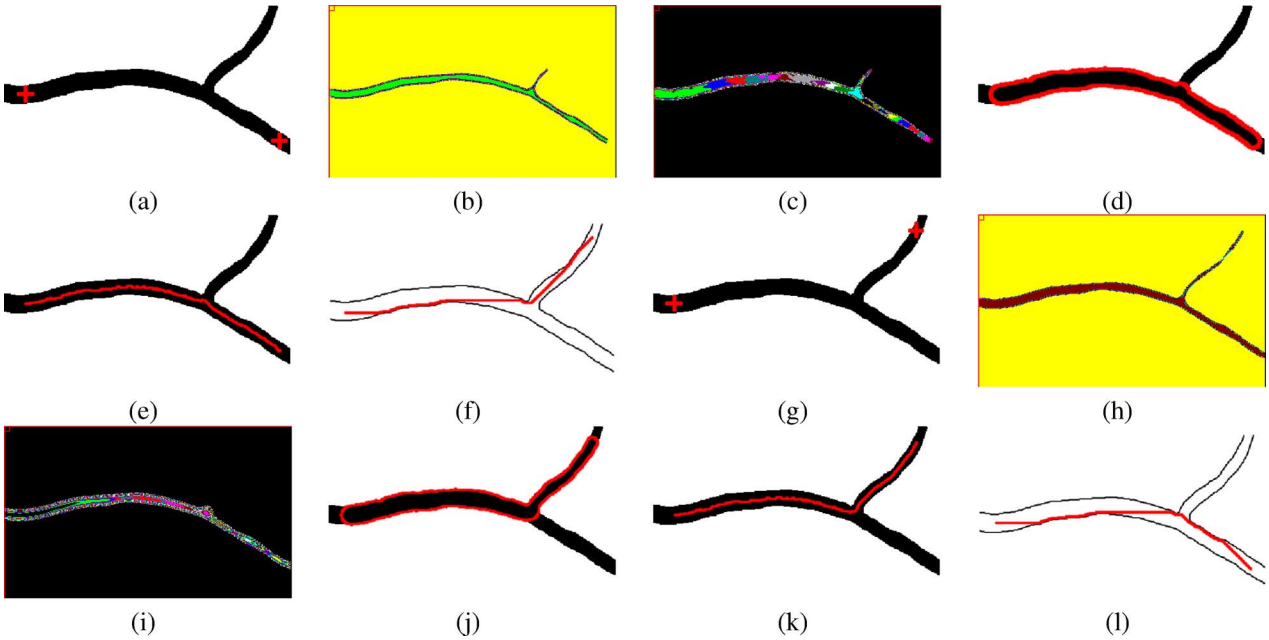

Fig. 3. Surface extraction results on a 2-D synthetic image. Panels (a) and (g) show the binary images with initializations. Centers of the initial spheres are shown with the red crosses. Panels (b) and (h) show the potential map with $r = 8$ and $r = 7$, respectively. Panels (c) and (i) show the distance map with $r = 8$ and $r = 12$. White lines in panels (d) and (j) show the surface extraction results from our method. Red lines in panels (e) and (k) show the extracted central paths from our method. Red lines in panels (f) and (l) show the path extraction results from the standard 2-D minimal path technique.

between the detected sphere and the starting sphere. These parameters should be selected based on the size and interior information of detected vessels, image noise levels, etc. As with any segmentation algorithm, the optimal set of parameters is very application dependent. In Fig. 5, we will illustrate the results of changing these parameters ω, λ_1, and λ_2.

This potential has two characteristics. First, it considers the mean and variance differences between the detected sphere and the starting sphere. If a sphere's radius is larger than the width of the tubular structure, the mean and variance differences between this sphere and the starting sphere will increase, and the related potential $\widetilde{P}$ will increase as well. Second, it also weights the mean and variance differences by r, which helps to ensure that the desired largest sphere also has lower potential than those smaller spheres inside the vessel. This sample potential satisfies the conditions discussed above, keeps the detected sphere as large as possible, is a region-based potential, and is suitable for extracting the vessel structures with constant interior intensities. We will use this potential to test the 2-D vessels shown in Sections III-A and III-B.

Three-dimensional vessels such as CTA coronary arteries are normally very thin and long with blurred boundaries and complex surrounding regions. In some cases, their intensities also may not be constant. Here, we design another example potential only based on the sphere's boundary information. First, we define $\partial B(p,r)$ as the boundary of sphere sp, and use it to replace $B(p,r)$ in (6). Then, we calculate the mean and variance only on the boundary of sphere sp. We also define the mean difference $\delta_\mu(sp)$ and the variance difference $\delta_{\sigma^2}(sp)$ between sphere $sp = (p,r)$ and sphere $sp' = (p, r-1)$ as

$$\delta_\mu(sp) = \left|\mu(sp) - \mu(sp')\right|, \quad \delta_{\sigma^2}(sp) = \left|\sigma^2(sp) - \sigma^2(sp')\right|. \tag{8}$$

The second sample potential, which also satisfies the condition discuss above, is designed as

$$\widetilde{P}(\hat{p}) = \widetilde{P}(sp) = w + \frac{\lambda_1}{1+\delta^2_{\mu(sp)}} + \frac{\lambda_2}{1+\delta^2_{\sigma^2(sp)}}. \tag{9}$$

Strictly speaking, these two sample potentials are all based on region information because every sphere in the original image is a small region. In order to improve the detection accuracy, we should decrease the potentials on the desired spheres as much as possible. The lower the potential on the desired sphere is, the higher the accuracy is. Because of the complexity and variety of medical images, it is hard to just use one specific potential to process all possible images, or find the suitable parameter setting for every specific image. Appropriate potentials should be chosen based on different image qualities, vessel structures, noise levels, and so on.

After deciding the potential, we can use the fast marching method [36] to solve (4) and obtain the minimal action map U. The algorithm complexity of the 4-D fast marching scheme is $O(N \log N)$, where N is the number of 4-D grid points. Furthermore, we may keep N small by limiting the range of the radius coordinate and discretizing it to just a few different values. We may also stop the fast marching evolution after we find the minimal action map at the end point instead of calculating it on the whole 4-D image space.

Since we represent the entire vessel as a 4-D curve on which each 4-D point represents a 3-D sphere, the 3-D vessel structure is then obtained as the envelope of the family of spheres traversed along this 4-D curve from noisy or low contrast 3-D data without the sensitivity to local minima inherent in most active surface techniques. Because all the spheres on the detected minimal "path" are tangential to the boundary of the tubular struc-

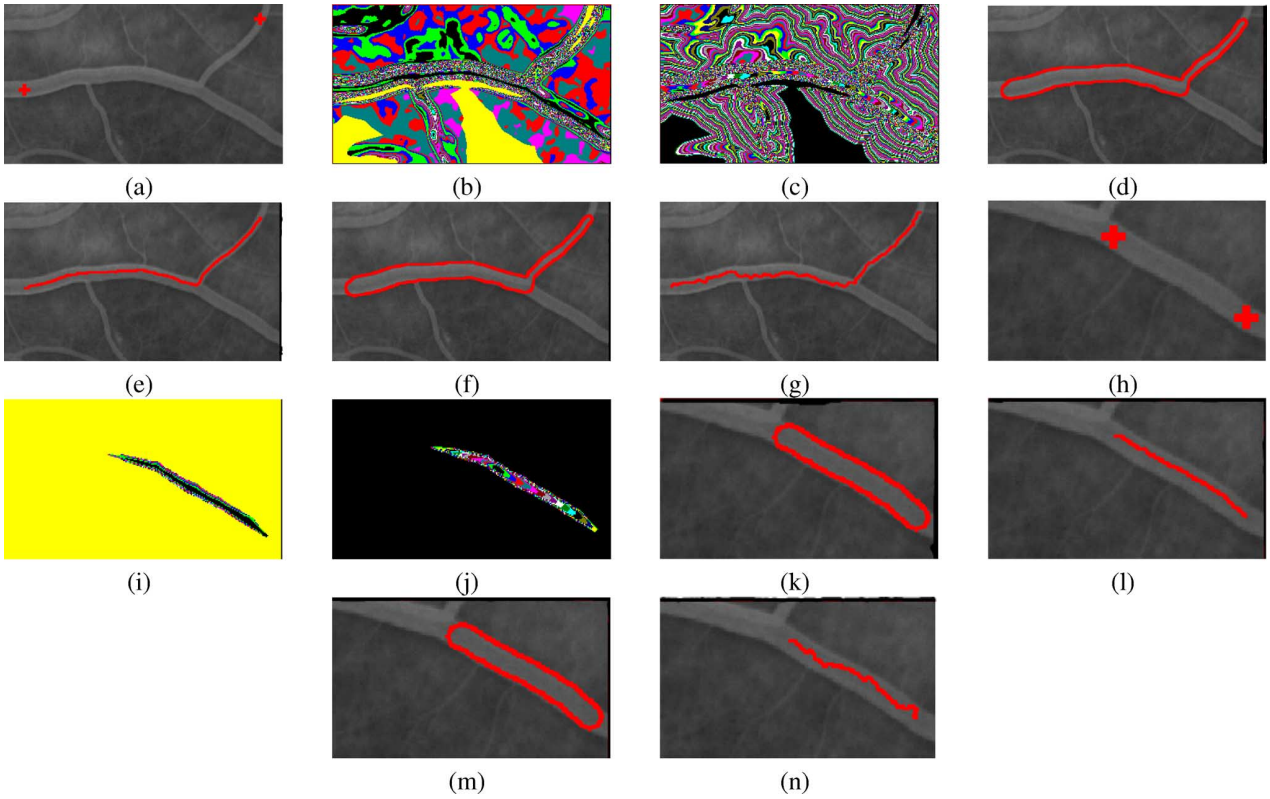

Fig. 4. Surface extraction results on two real angiogram images. Centers of the initial spheres are shown with the red crosses. Panels (a) and (h) show the original images with initializations. Panels (b) and (i) show the potential maps with $r = 10$ and $r = 8$, respectively. Panels (c) and (j) show the distance maps with $r = 10$ and $r = 8$, respectively. Red lines in panels (d) and (k) show the surface extraction results from our method. Red lines in panels (e) and (l) show the extracted central paths from our method. Red lines in panels (f) and (m) show the surface extraction results from our method with a large maximum radius $r_{\max} = 40$. Red lines in panels (g) and (n) show the path extraction results from the standard 2-D minimal path technique.

ture, the union of their center points describes the central path of the tubular structure. We, therefore, obtain the centered path by tracing the center points of the family of 3-D spheres rather than its envelope. Furthermore, the classical minimal path technique can be treated as a special case of our method by setting the sphere radius to 0. However, as demonstrated in the upcoming experiments, it is much better to perform the minimal path procedure fully in 4-D in order to obtain the actual vessel surfaces as well as their central paths.

III. Experimental Results and Analysis

In this section, we test our approach on various 2-D and 3-D simulated and real images. For each test, users need to specify the center points and radii at the starting and ending points, the potential, and the largest allowed radius of the tubular object. Four probabilities

$$\mathrm{TP} = \frac{N_B \cap N_R}{N_R}, \quad \mathrm{FN} = \frac{N_R - N_B \cap N_R}{N_R},$$
$$\mathrm{FP} = \frac{N_B - N_B \cap N_R}{N_R}, \quad \mathrm{OM} = 2 \cdot \frac{N_B \cap N_R}{N_B + N_R}, \quad (10)$$

are defined for validation. N_R is the number of reference ground truth voxels of vessel T. N_B is the number of voxels detected by our algorithm for vessel T. TP, FN, and FP are the true positive, false negative, and false positive parameters. OM means overlap metric which is a Dice similarity coefficient [46] and approaches a value of 1.0 for results that are very similar and is near 0.0 when they share no similarly classified voxels.

A. Experiments on 2-D Images

In Fig. 3, we first present the segmentation results on a 2-D binary image with two different pairs of initial spheres. The image size is 350×200. The radii of the left and right spheres and the largest allowed radius are set to $r_{\text{left}} = 12$, $r_{\text{right}} = 7$, and $r_{\max} = 15$ in Fig. 3(a), while $r_{\text{left}} = 12$, $r_{\text{right}} = 8$, and $r_{\max} = 15$ in Fig. 3(g). For these two segmentations, we use the potential defined by (7) with $\omega = 10$, $\lambda_1 = 10$, and $\lambda_2 = 10$. The computational times are about 1 s for both tests. We also show the corresponding potential maps $\widetilde{P}$ which have lower values on desired 3-D locations, and the minimal action maps U which show the gradient descent along the desired 3-D path.

In Fig. 4, we present the segmentation results on the real 2-D noisy projections of two angiograms with two different initializations (obviously, one should segment the 3-D data, but here we can illustrate the accuracy of the result since the full 2-D curve may be superimposed on the 2-D projection image data). The image sizes are 350×200. In Fig. 4(a), we set $r_{\text{left}} = 10$, $r_{\text{right}} = 2$, and $r_{\max} = 15$. In Fig. 4(h), we set $r_{\text{left}} = 8$, $r_{\text{right}} = 8$, and $r_{\max} = 15$. For these two segmentations, we use the potential defined by (7) with $\omega = 10$, $\lambda_1 = 10$, and $\lambda_2 = 10$. The computational times are around 3 s.

In our method, parameters $\widetilde{P}$, r_{left}, r_{right}, and $r_{\max}$ may affect the final results. In Section II-C, we briefly discussed how

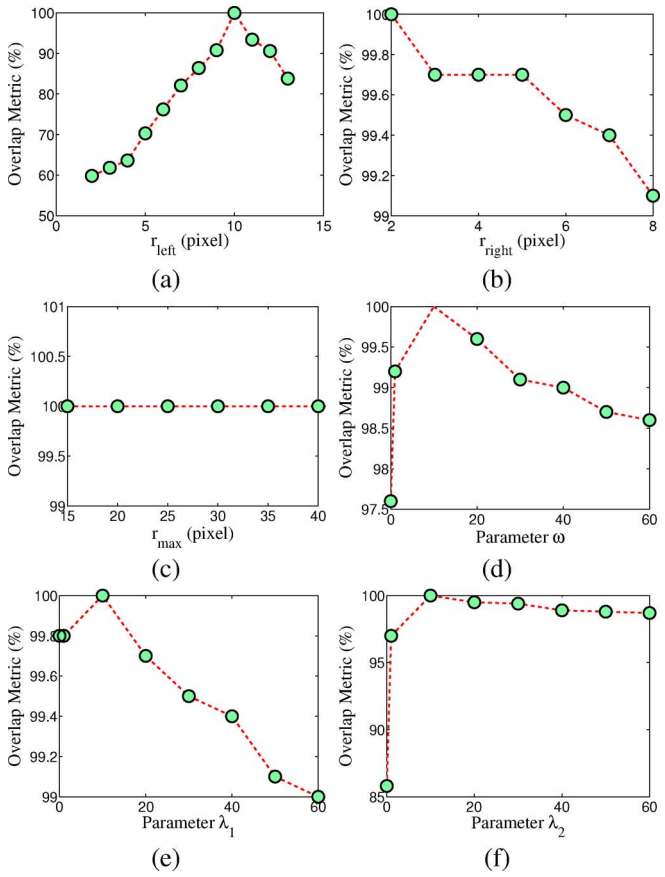

Fig. 5. Comparison of the segmentation results obtained by changing parameters r_{left}, r_{right}, $r_{\max}$, ω, λ_1, and λ_2, respectively.

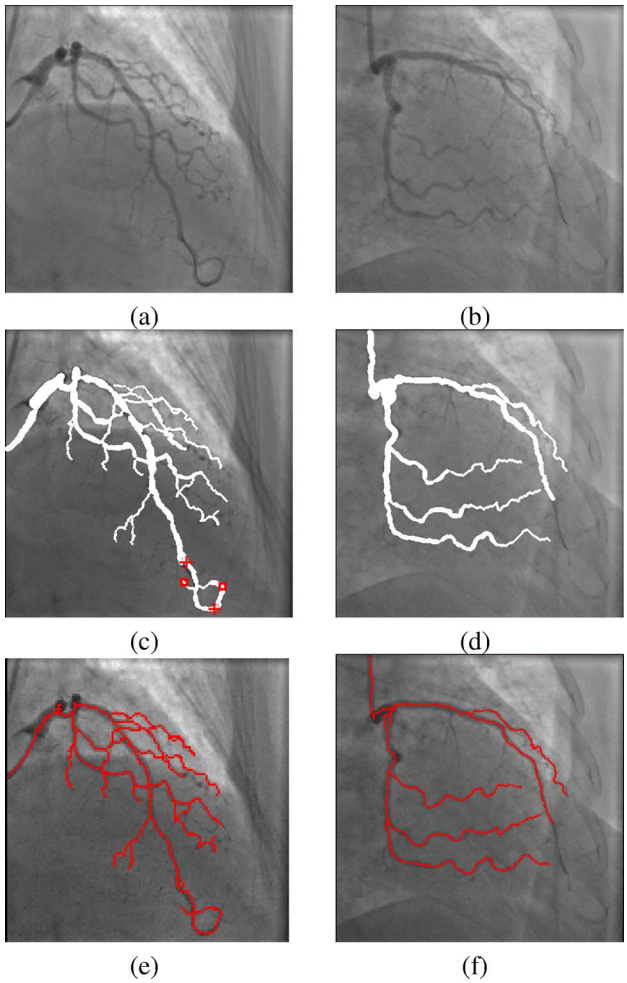

Fig. 6. Surface and central line extraction results on two 2-D MRA images. Panels (a) and (b) show the original images. Panels (c) and (d) show the extracted vessel surfaces by our method. Panels (e) and (f) show the extracted central lines by our method.

to choose the potentials for different images. Here, we illustrate the influence of the parameters r_{left}, r_{right}, $r_{\max}$, ω, λ_1, and λ_2 onthe segmentation results. We use the image in Fig. 4(a) as a sample for this test and compare the results in Fig. 5. In order to test r_{left}, r_{right}, and $r_{\max}$ (measured by pixels), we fix the locations of two initial points and the potential defined in (7), and only change these three parameters independently. We choose the result based on $r_{\text{left}} = 10$, $r_{\text{right}} = 2$, $r_{\max} = 15$, $\omega = 10$, $\lambda_1 = 10$, and $\lambda_2 = 10$ as the standard and compare it with other results. Because it is impossible for us to test all of the combinations of these three parameters, we choose a certain range [2–13] for r_{left}, [2–8] for r_{right}, and [15,20,25,30,35,40] for $r_{\max}$. One of these three parameters varies independently and the other two are fixed as the standard values for each test. We use the overlap metric OM defined in (10) to measure the similarity between each result and the standard. Similarly, when testing ω, λ_1, and λ_2, we fix $r_{\text{left}} = 10$, $r_{\text{right}} = 2$, $r_{\max} = 15$, and choose the result based on $\omega = 10$, $\lambda_1 = 10$, and $\lambda_2 = 10$ as the standard and compare it with other results. ω, λ_1, and λ_2 all vary in a range [0,1,10,20,30,40,50,60] respectively.

As can be seen in Fig. 5(a), changing r_{left} does change the results dramatically because r_{left} relates to the starting point. Changing r_{right} [shown in Fig. 5(b)] only changes the results slightly, On the other hand, when changing $r_{\max}$ [shown in Fig. 5(c)], the segmentation results do not change from the assumed standard result because the value of $r_{\max}$ does not affect the energy functionals of global minimal path methods. This observation shows that choosing appropriate radii of initial spheres r_{left} and r_{right} is much more important than choosing $r_{\max}$. For an image with blurred vessel boundaries, because it is hard to decide the correct radii of the initial spheres, the final results will change when the radii of the initial spheres change. Although theoretically, changing the maximum radius does not and should not induce a dramatic effect on results, we still suggest choosing an appropriate $r_{\max}$ for each processed image, because an unreasonably big maximum radius may increase the possibility of errors and also increase the running time of the fast marching evolution schemes. As can be seen in Fig. 5(d) and (e), when changing ω, λ_1, and λ_2, the segmentation results do not change significantly from the assumed standard. The reason is that ω controls the smoothness of obtained paths, and should not change the vessel width and shape much. In this test, changing λ_1 and λ_2 does not change results dramatically. However, for detecting noisy vessel structures, we should decrease the weight on the variance difference.

In Fig. 6, we present the segmentation results on two other real 2-D noisy angiogram projection images. For this test, we set several pairs of initial radii. For each pair of radii, we use the mouse to choose the locations of two initial points and obtain the vessel between them, then combine all the detected vessels to get the final result. We still use the potential defined by (7)

TABLE I
COMPARISONS OF THE 2-D RETINAL IMAGE SEGMENTATION RESULTS OF OUR METHOD WITH THE GROUND TRUTH DATA

Rate	2D test images				
	1	2	3	4	5
TP (%)	79.8	82.0	81.0	83.1	79.9
FN (%)	20.2	18.0	19.0	16.9	20.1
FP (%)	19.6	16.5	20.4	15.4	19.5
OM	0.800	0.826	0.804	0.837	0.801

(a) (b) (c)

Fig. 7. Surface extraction result on one of the five cropped 2-D retinal images tested in Table I. Panels (a) show the original retinal image. Panels (b) show the extraction result from our method. Panels (c) show the overlap pixels and difference pixels between our result and the manual segmentation. Pixels in red color are the overlap pixels between our results and the manual segmentations. Pixels in blue color are the pixels which are detected by the manual segmentations but not by our method. Pixels in green color are the pixels which are detected by our method but not by the manual segmentations.

with $\omega = 10$, $\lambda_1 = 10$, and $\lambda_2 = 10$. Notice that in Fig. 6(c), one branch of the vessel structure is self-intersecting. For extracting this structure, we choose three pairs of initializations [shown in Fig. 6(c)]. Unlike some topology-preserving active contour models, our method does not consider the topological information of vessels, and it always finds the shortest path between two initial points. By choosing appropriate initial spheres, our method can detect self-intersecting curves easily.

B. Quantitative Evaluation on 2-D Images

The quantitative evaluation results of our algorithm on 2-D images are given in Table I and Fig. 7. We validate our approach on five cropped retinal images provided by the DRIVE [47] database. The DRIVE database consists of 40 color retinal images captured from a Canon CR5 nonmydriatic 3CCD camera with a 45° field-of-view (FOV). The images are all 768 × 584 pixels and 8 bits per color plane. The FOV of each image is approximately 540 pixels in diameter, and each image has been cropped around the FOV. In this database, all 40 images have been divided into a training set and a test set. Each set contains 20 images. One manual segmentation is provided for the images in the training set. Two manual segmentations are available for the test set: one is used as gold standard, and the other serves as an independent human observer reference for comparisons with computer generated segmentations.

The main purpose for our test on these five images is to quantitatively analyze the accuracy of the proposed algorithm. Considering the properties of our method, the complexity of retinal images, and the purpose of this test, we cropped these five different parts from three retinal images, and tested our method directly on them. We still use the potential defined by (7) with $\omega = 10$, $\lambda_1 = 10$, and $\lambda_2 = 10$ to test these five images. As in Fig. 6, we set several pairs of initial radii. For each pair of radii, we used the mouse to choose two initial point locations and obtain the vessel between them, then combined all the detected vessels to get the final result. As revealed in Table I, our method obtains a truth positive ranging from 79.8% to 83.1%, with overlap metrics over 0.8. There are three main reasons which induce the errors. First, our method is a sphere-based algorithm, when we convert the obtained minimal paths in a higher dimension space to the vessel surfaces in the actual vessel space, it is hard to set accurate spheres for very thin retinal vessels which are only 2–3 pixels wide. Second, the ground truth data sets are discretized and rely on the image resolution, which are not strictly "tubes." Furthermore, these spheres are measured by pixels in our tests, as such the diameters of the spheres are always odd numbers, but in the ground truth data, the diameters of some vessels are even numbers, this induces the differences between our results and the ground truth data. Third, the quality of these testing images is not very good, and the original images are very blurred, it is hard to set the most appropriate initial radii for the initial spheres. As discussed in Fig. 5, the radii of the initial spheres may affect the final results.

C. Experiments on 3-D Images

The proposed method is very easy to extend to three dimensions. In this subsection, we test our method on several 3-D CTA or MRA images for further evaluation under more realistic conditions.

In Fig. 8, we test the method on a 3-D CT dataset of the coronary artery. For this test, we set $r_0 = 4$, $r_1 = 1$, and $r_{\max} = 7$ for segmenting the left anterior descending artery (also obtaining part of the left main coronary artery) and the left obtuse marginal artery, $r_0 = 3$, $r_1 = 1$, and $r_{\max} = 7$ for segmenting the left circumflex artery with a subbranch, $r_0 = 1$, $r_1 = 1$, and $r_{\max} = 5$ for segmenting the subbranch of the left obtuse marginal artery. The potential is defined by (9) with $\omega = 10$, $\lambda_1 = 10$, and $\lambda_2 = 10$.

In Fig. 9, we show the extraction of an ascending aorta from the 3-D CT dataset of a coronary artery and the extraction of brain vasculatures from a 3-D brain MRA image. Normally, ascending aortas and MRA brain vessels are wider than coronary arteries. These tests illustrate that the bigger the actual vessel sizes are, the smoother the extraction results. The image size in Fig. 9(a) is $110 \times 90 \times 80$. The potential is defined by (9) with $\omega = 1$, $\lambda_1 = 10$, and $\lambda_2 = 10$. $r_0 = 25$, $r_1 = 25$, and $r_{\max} = 30$ are set for the initial spheres. For improving the computation time, we set a new parameter $r_{\min} = 20$, and search r in this narrow range $r_{\min} \leq r \leq r_{\max}$ instead of $0 \leq r \leq r_{\max}$. The computation time is less than 2 min. The image size in Fig. 9(c) is $80 \times 120 \times 280$. The potential is defined by (9) with $\omega = 1$, $\lambda_1 = 10$, and $\lambda_2 = 10$.

D. Quantitative Evaluation on 3-D Images

Contrary to the experiments shown in Fig. 7 and Table I, it is very difficult to obtain the ground truth data for validating the 3-D segmentation results. In Fig. 10 and Table II, we show the comparison between the results obtained from our method and results acquired manually. We test our method directly on five 3-D clinical CTA coronary datasets without any preprocessing.

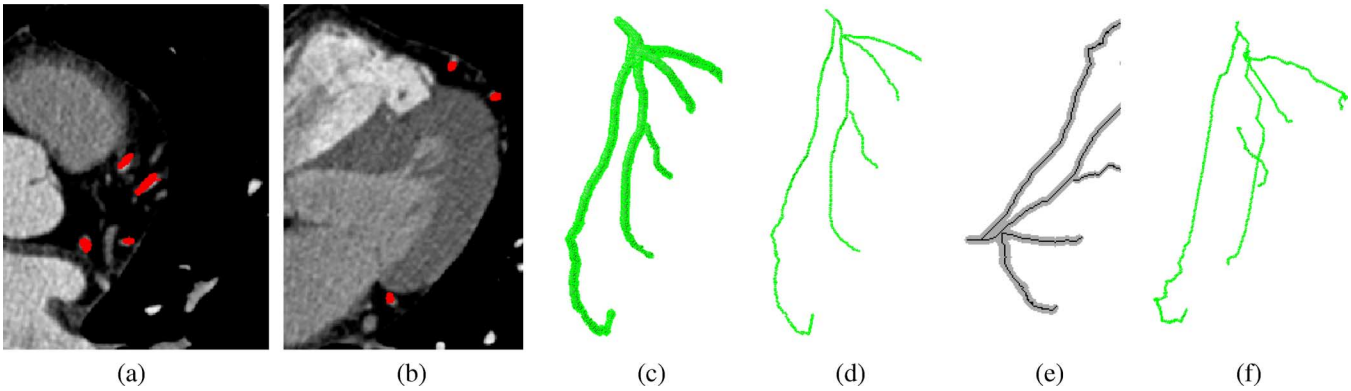

Fig. 8. Segmentation result of the left main coronary artery on a 3-D CT image. Panels (a) and (b) show the segmentation results on two 2-D slices from our method. Panel (c) shows the reconstructed 3-D model of the segmented left main coronary artery, the left anterior descending artery, the left obtuse marginal artery with one subbranch, and the left circumflex artery with a subbranch from our method. Panel (d) shows the 3-D model of the corresponding central path from our method. Panel (e) shows the projection of the segmented 3-D surface and the central path from our method. For comparison, panel (f) show the minimal path results from the standard 3-D minimal path technique [10]. The potential is $\widetilde{P}(p) = 10 + |\nabla I(p)|^2$ for panel (f). $|\nabla I(p)|$ is the image gradient magnitude.

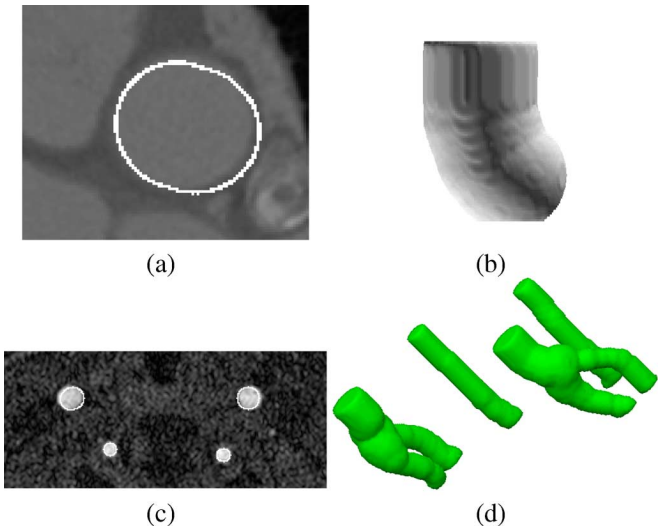

Fig. 9. Part of the aorta extraction results from a 3-D CT image, and the brain vessel extraction results from a brain MRA image. Panels (a) and (c) show the results on each slice of these two images, respectively. Panels (b) and (d) show the reconstructed 3-D models.

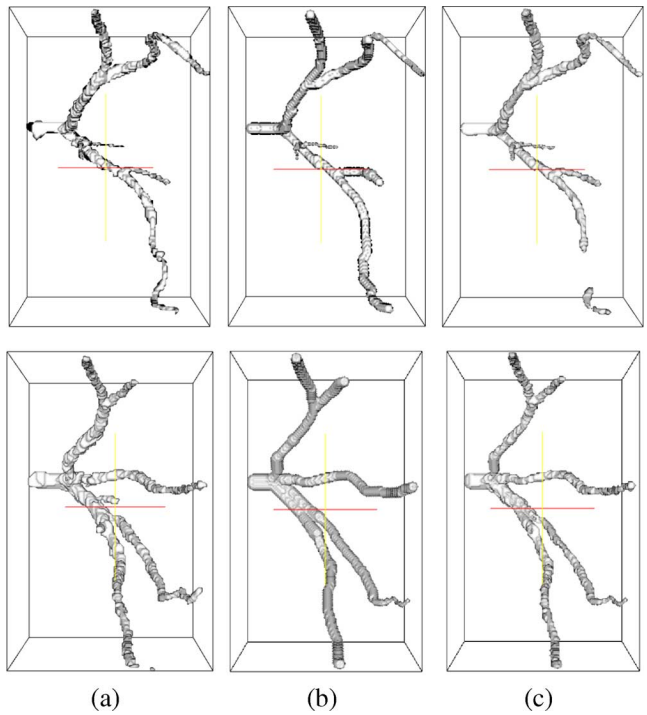

Fig. 10. Segmentation results on two of the five real CTA images based on our method. Panel (a) shows the manual segmentation results. Panel (b) shows the segmentation results of our method. Panel (c) shows the overlap voxels between our results and the manual segmentations.

The potential is defined by (9) with $\omega = 1$, $\lambda_1 = 10$, and $\lambda_2 = 10$.

One of these five manual drawings was contoured by a physician at Emory University, Atlanta, GA, the other four were contoured by a biomedical student who was trained by the physician. These manual results were obtained by hand drawing on every 2-D slice. This procedure is very time consuming and subjective, and also has several other drawbacks. First, the 3-D vessel structure information is not referenced during the drawing process, so the manual results are not smooth. In particular, some small and thin vessels may appear broken or disconnected from larger branches. Second, the manual drawing only based on mouse clicks always generates too many errors. Thus, the manual segmentations with which we compare our method cannot be considered as an ideal ground truth. The thin structures that our method obtained go beyond those obtained by the manual method [the most severe case is shown in the first row of Fig. 10(c)]. These additional pieces constitute the main factor that increases the false positive (FP). But this comparison also shows that our method can correctly detect almost all branches and also reduce user-interaction while having the ability to segment thin vessels. Since our method is a 4-D minimal path technique, it is better able to extract continuous and smooth 3-D arteries from the surrounding region.

Using the manual segmentation results of these five CTA images, we also validate our method on 15 noisy simulated CTA images, which are produced from the manual segmentations by adding different noise levels to them. After discussion with medical physicists and by referring to [40], we created five noisy images by adding Gaussian noise with standard deviation $\sigma = 20$,

TABLE II
COMPARISONS OF THE 3-D CORONARY IMAGE SEGMENTATION RESULTS OF OUR METHOD WITH THE MANUAL SEGMENTATIONS

Rate	3D test images				
	1	2	3	4	5
TP (%)	62.7	75.2	68.3	74.4	42.5
FN (%)	37.3	24.8	31.7	25.6	57.5
FP (%)	41.4	71.3	42.0	91.9	30.7
OM	0.614	0.610	0.649	0.558	0.491

TABLE III
COMPARISONS OF THE 15 3-D NOISY SIMULATED IMAGE SEGMENTATION RESULTS WITH THE MANUAL SEGMENTATIONS

Rate	3D test images				
	1	2	3	4	5
OM ($\sigma = 20$)	0.689	0.692	0.702	0.678	0.715
OM ($\sigma = 40$)	0.557	0.571	0.564	0.565	0.584
OM ($\sigma = 80$)	0.489	0.487	0.472	0.449	0.537

a representative noise level in MR and CT data, to these five manual segmentations. Furthermore, in order to observe the performance of our method in worse situations, we also created 10 noisy images by adding Gaussian noise with higher standard deviations $\sigma = 40$ and $\sigma = 80$, respectively. Then the same initial point pairs and potentials in Table II are used to test these 15 noisy images, and the overlap metrics are shown in Table III. This validation demonstrates that real images are more difficult to be segmented accurately compared to the simulated images with a reasonable noise level $(\sigma = 20)$. Simulated images do provide the advantage that the ground-truth data is known and thus the performance of the segmentation method can be objectively measured. However, it may not necessarily reflect all physiological and imaging variability and effects of real images.

IV. CONCLUSIONS AND FUTURE WORK

In this paper, we present a novel 3-D tubular surface extraction method that not only keeps all of the benefits of standard minimal path techniques, but also combines some of the benefits of active surface techniques by representing the full 3-D tubular surface rather than a just curve within its interior. We are able to fully exploit minimal path techniques to obtain the global minimizing trajectory between two user supplied endpoints in order to reconstruct a vessel from noisy or low contrast 3-D data, and also yield the central path of the tubular structure simultaneously. We chose coronary artery segmentation as one of the many possible illustrative 3-D experiments, showing that this new technique can extract 3-D tubular structures and their corresponding center lines more accurately than the classical minimal path techniques. In order to emphasize these properties, we tested the proposed method directly on the original (unpreprocessed) 2-D and 3-D images with extremely simple initializations (just spheres). We also compared our results with the ground truth data (2-D retinal images) and the manual segmentation results (3-D CTA coronary images). After the 3-D tubular surface is found, it can provide direct visualization of coronary arteries over a long stretch of vessel. Furthermore, it can be used as a preprocessing step in the quantitative analysis of vessel morphology and can provide more useful information for clinical applications such as vessel disease detection, aneurysm detection and analysis.

In the future, we hope to expand the proposed method to extract objects with different shapes such as an abnormal vessel (for example, an aneurysm) by using different underlying structural elements (such as ellipses) rather than spheres. Beyond the application to medical vessel images, the proposed method can also be applied to extract other tubular structures such as roads and plant roots, and thus has great potential for tubular surface analysis in other fields as well.

ACKNOWLEDGMENT

The authors would like to thank the anonymous reviewers for valuable comments and suggestions. They would like to thank Dr. Y. Yang and Dr. J. Suo at Georgia Institute of Technology, Atlanta, for providing some original images and manual segmentations. They would also like to thank G. Sundaramoorthi of School of Electrical and Computer Engineering, Georgia Institute of Technology, Atlanta, for his helpful discussion.

REFERENCES

[1] L. Clarke, R. Velthuizen, M. Camacho, J. Heine, M. Vaidyanathan, L. Hall, R. Thatcher, and M. Silbiger, "MRI segmentation: Methods and applications," *Magnetic Resonance Imag.*, vol. 13, no. 3, pp. 343–368, 1995.

[2] T. McInerney and D. Terzopoulos, "Deformable models in medical image analysis: A survey," *Med. Image Anal.*, vol. 1, no. 2, pp. 91–108, 1996.

[3] J. Duncan and N. Ayache, "Medical image analysis: Progress over two decades and the challenges ahead," *IEEE Trans. Pattern Anal. Mach. Intell.*, vol. 22, no. 1, pp. 85–105, Jan. 2000.

[4] D. Pham, C. Xu, and J. Prince, "Current methods in medical image segmentation," *Annu. Rev. Biomed. Eng., Annu. Rev.*, vol. 2, pp. 315–337, 2000.

[5] C. Kirbas and F. Quek, "A review of vessel extraction techniques and algorithms," *ACM Comput. Surveys (CSUR)*, vol. 36, no. 2, pp. 81–121, 2004.

[6] M. Kass, A. Witkin, and D. Terzopoulos, "Snakes: Active contour models," *Int. J. Comput. Vis.*, vol. 1, no. 4, pp. 321–332, 1988.

[7] A. Yezzi, S. Kichenassamy, A. Kumar, P. Olver, and A. Tannenbaum, "A geometric snake model for segmentation of medical imagery," *IEEE Trans. Med. Imag.*, vol. 16, no. 2, pp. 199–209, Apr. 1997.

[8] V. Caselles, R. Kimmel, and G. Sapiro, "Geodesic active contours," *Int. J. Comput. Vis.*, vol. 22, no. 1, pp. 61–79, 1997.

[9] L. Cohen and R. Kimmel, "Global minimum for active contour models: A minimal path approach," in *Proc. IEEE Int. Conf. Comput. Vis. Pattern Recognit.*, Jun. 1996, pp. 666–673.

[10] L. Cohen and R. Kimmel, "Global minimum for active contour models: A minimal path approach," *Int. J. Comput. Vis.*, vol. 24, no. 1, pp. 57–78, 1997.

[11] A. Frangi, W. Niessen, R. Hoogeveen, T. van Walsum, and M. Viergever, "Model-based quantitation of 3-D magnetic resonance angiographic images," *IEEE Trans. Med. Imag.*, vol. 18, no. 10, pp. 946–956, Oct. 1999.

[12] L. Lorigo, O. Faugeras, W. Grimson, R. Keriven, R. Kikinis, A. Nabavi, and C. Westin, "CURVES: Curve evolution for vessel segmentation," *Med. Image Anal.*, vol. 5, no. 3, pp. 195–206, 2001.

[13] C. V. Bemmel, L. Spreeuw, M. Viergever, and W. Niessen, "Level set based artery vein separation in blood pool agent CE-MR angiograms," *IEEE Trans. Med. Imag.*, vol. 22, no. 10, pp. 1224–1234, Oct. 2003.

[14] L. Antiga, B. Ene-Iordache, and A. Remuzzi, "Computational geometry for patient-specific reconstruction and meshing of blood vessels from MR and CT angiography," *IEEE Trans. Med. Imag.*, vol. 22, no. 5, pp. 674–684, May 2003.

[15] J. Chen and A. Amini, "Quantifying 3-D vascular structures in MRA images using hybrid PDE and geometric deformable models," *IEEE Trans. Med. Imag.*, vol. 23, no. 10, pp. 1251–1262, Oct. 2004.

[16] P. Yim, G. Vasbinder, V. Ho, and P. Choyke, "Isosurfaces as deformable models for magnetic resonance angiograpy," *IEEE Trans. Med. Imag.*, vol. 22, no. 7, pp. 875–881, Jul. 2003.

[17] Y. Yang, A. Tannenbaum, and D. Giddens, "Knowledge-based 3-D segmentation and reconstruction of coronary arteries using CT images," in *Proc. 26th Annu. Int. Conf. IEEE Eng. Med. Biol. Soc.*, Sep. 2004, vol. 3, pp. 1664–1666.

[18] D. Nain, A. Yezzi, and G. Turk, "Vessel segmentation using a shape driven flow," in *Proceedings of 7th International Conference of Medical Image Computing and Computer-Assisted Intervention (MICCAI)*. Berlin, Germany: Springer Verlag, 2004, vol. 3216, Lecture Notes in Computer Science, pp. 51–59.

[19] R. Manniesing, B. Velthuis, M. van Leeuwen, I. van der Schaaf, P. van Laar, and W. Niessen, "Level set based cerebral vasculature segmentation and diameter quantification in CT angiography," *Med. Image Anal.*, vol. 10, no. 2, pp. 200–214, 2006.

[20] P. Yan and A. Kassim, "Segmentation of volumetric MRA images by using capillary active contour," *Med. Image Anal.*, vol. 10, no. 3, pp. 317–329, 2006.

[21] D. Wilson and J. Noble, "An adaptive segmentation algorithm for time-of-flight MRA data," *IEEE Trans. Med. Imag.*, vol. 18, no. 10, pp. 938–945, Oct. 1999.

[22] M. de Bruijne, B. van Ginneken, M. A. Viergever, and W. J. Niessen, "Adapting active shape models for 3-D segmentation of tubular structures in medical images," in *18th Int. Conf. Inf. Process. Med. Imag. (IPMI)*, 2003, pp. 136–147.

[23] G. Gerig, O. Kbler, R. Kikinis, and F. Jolesz, "Nonlinear anisotropic filtering of MRI Data," *IEEE Trans. Med. Imag.*, vol. 11, no. 2, pp. 221–232, Jun. 1992.

[24] Y. Sato, J. Chen, R. Zoroofi, N. Harada, S. Tamura, and T. Shiga, "Automatic extraction and measurement of leukocyte motion in microvessels using spatiotemporal image analysis," *IEEE Trans. Biomed. Eng.*, vol. 44, no. 4, pp. 225–236, Apr. 1997.

[25] M. Sonka, G. Reddy, M. Winniford, and S. Collins, "Adaptive approach to accurate analysis of small-diameter vessels in cineangiograms," *IEEE Trans. Med. Imag.*, vol. 16, no. 1, pp. 87–95, Feb. 1997.

[26] A. Wahle, E. Wellnhofer, I. Mugaragu, H. Saner, H. Oswald, and E. Fleck, "Assessment of diffuse coronary artery disease by quantitative analysis of coronary morphology based upon 3-D reconstruction from biplane angiograms," *IEEE Trans. Med. Imag.*, vol. 14, no. 2, pp. 230–241, Jun. 1995.

[27] P. Yim, P. Choyke, and R. Summers, "Gray-scale skeletonization of small vessels in magnetic resonance angiography," *IEEE Trans. Med. Imag.*, vol. 19, no. 6, pp. 568–576, Jun. 2000.

[28] S. Wan and W. Higgins, "Symmetric region growing," *IEEE Trans. Image Process.*, vol. 12, no. 9, pp. 1007–1015, Sep. 2003.

[29] S. Olabarriaga, M. Breeuwer, and W. Niessen, "Minimum cost path algorithm for coronary artery central axis tracking in CT images," in *Proceedings of 6th International Conference of Medical Image Computing and Computer-Assisted Intervention (MICCAI)*. Berlin, Germany: Springer, 2003, vol. 2879, Lecture Notes in Computer Science, pp. 687–694.

[30] N. Passat, C. Ronse, J. Baruthio, J. Armspach, and C. Maillot, "Magnetic resonance angiography: From anatomical knowledge modeling to vessel segmentation," *Med. Image Anal.*, vol. 10, no. 2, pp. 259–274, 2006.

[31] O. Wink, W. Niessen, and M. Viergever, "Multiscale vessel tracking," *IEEE Trans. Med. Imag.*, vol. 23, no. 1, pp. 130–133, Jan. 2004.

[32] E. Dijkstra, "A note on two problems in connection with graphs," *Numerische Math.*, vol. 1, pp. 269–271, 1959.

[33] S. Bouix, K. Siddiqi, and A. Tannenbaum, "Flux driven automatic centerline extraction," *Med. Image Anal.*, vol. 9, no. 3, pp. 209–221, 2005.

[34] K. Siddiqi, S. Bouix, A. Tannenbaum, and S. Zucker, "Hamilton-Jacobi skeletons," *Int. J. Comput. Vis.*, vol. 48, no. 3, pp. 215–231, 2002.

[35] T. Deschamps and L. Cohen, "Fast extraction of minimal paths in 3-D images and applications to virtual endoscopy," *Med. Image Anal.*, vol. 5, no. 4, pp. 281–299, 2001.

[36] J. Sethian, "Fast marching methods," *SIAM Rev.*, vol. 41, no. 2, pp. 199–235, 1999.

[37] S. Wan, A. Kiraly, E. Ritman, and W. Higgins, "Extraction of the hepatic vasculature in rats using 3-D micro-CT images," *IEEE Trans. Med. Imag.*, vol. 19, no. 9, pp. 964–971, Sep. 2000.

[38] K. Mori, J. Hasegawa, Y. Suenaga, and J. Toriwaki, "Automated anatomical labeling of the bronchial branch and its application to the virtual bronchoscopy system," *IEEE Trans. Med. Imag.*, vol. 19, no. 2, pp. 103–114, Feb. 2000.

[39] K. Krissian, G. Malandain, N. Ayache, R. Vaillant, and Y. Trousset, "Model-based detection of tubular structures in 3-D images," *Comput. Vis. Image Understand.*, vol. 80, no. 2, pp. 130–171, 2000.

[40] S. Aylward and E. Bullitt, "Initialization, noise, singularities, and scale in height ridge traversal for tubular object centerline extraction," *IEEE Trans. Med. Imag.*, vol. 21, no. 2, pp. 61–75, Feb. 2002.

[41] D. Adalsteinsson and J. Sethian, "A fast level set method for propagating interfaces," *J. Computational Phys.*, vol. 118, no. 2, pp. 269–277, 1995.

[42] E. Rouy and A. Tourin, "A viscosity solutions approach to shape-from-shading," *SIAM J. Numer. Anal.*, vol. 29, no. 3, pp. 867–884, 1992.

[43] P. Dupuis and J. Oliensis, "An optimal control formulation and related numerical methods for a problem in shape reconstruction," *Ann. Appl. Probabil.*, vol. 4, no. 2, pp. 287–346, 1994.

[44] J. Sethian, "A fast marching level set method for monotonically advancing fronts," *Proc. Nat. Acad. Sci. USA*, vol. 93, no. 4, pp. 1591–1595, 1996.

[45] R. Ardon and L. Cohen, "Fast constrained surface extraction by minimal paths," in *Int. Conf. Comput. Vis.-Workshop VLSM*, 2003, pp. 233–244.

[46] A. Zijdenbos, B. Dawant, R. Margolin, and A. Palmer, "Morphometric analysis of white matter lesions in MR images: Methods and validation," *IEEE Trans. Med. Imag.*, vol. 13, no. 4, pp. 716–724, Dec. 1994.

[47] J. Staal, M. Abramoff, M. Niemeijer, M. Viergever, and B. van Ginneken, "Ridge based vessel segmentation in color images of the retina," *IEEE Trans. Med. Imag.*, vol. 23, no. 4, pp. 501–509, Apr. 2004.